

# A terahertz vibrational molecular clock with systematic uncertainty at the $10^{-14}$ level

K. H. Leung,<sup>1,\*</sup> B. Iritani,<sup>1,\*</sup> E. Tiberi,<sup>1</sup> I. Majewska,<sup>2,†</sup> M. Borkowski,<sup>1,3</sup> R. Moszynski,<sup>2</sup> and T. Zelevinsky<sup>1,‡</sup>

<sup>1</sup>*Department of Physics, Columbia University, 538 West 120th Street, New York, NY 10027-5255, USA*

<sup>2</sup>*Quantum Chemistry Laboratory, Department of Chemistry, University of Warsaw, Pasteura 1, 02-093 Warsaw, Poland*

<sup>3</sup>*Institute of Physics, University of Amsterdam, Science Park 904, 1098XH Amsterdam, The Netherlands*

(Dated: September 29, 2022)

Neutral quantum absorbers in optical lattices have emerged as a leading platform for achieving clocks with exquisite spectroscopic resolution. However, the class of absorbers and studies of systematic shifts in these clocks have so far been limited to atoms. Here, we extend this architecture to an ensemble of diatomic molecules and experimentally realize an accurate lattice clock based on pure molecular vibration. We evaluate the leading systematics, including the characterization of nonlinear trap-induced light shifts, achieving a total systematic uncertainty of  $4.5 \times 10^{-14}$ . The absolute frequency of the vibrational splitting is measured to be 31 825 183 207 601.1(3.3) Hz, enabling the dissociation energy of our molecule to be determined with record accuracy. Our results represent an important milestone in molecular spectroscopy, THz frequency standards, and may be generalized to other neutral molecular species with applications for fundamental physics, including tests of molecular quantum electrodynamics and the search for new interactions.

## I. INTRODUCTION

The pursuit of high performance quantum clocks has historically spurred important developments, including laser cooling [1–3] and optical trapping [4, 5]. In one highly successful clock architecture, large numbers of quantum absorbers are tightly confined in a magic wavelength optical lattice, affording reduced quantum projection noise [6]. Such lattice clocks, so far employing atomic optical transitions, have realized record performance in both precision [7–12] and accuracy [11–17], ushering in a new era in space-time sensing [18–21]. In parallel, there is growing interest in advancing the laser spectroscopy and quantum control of more complex particles—such as diatomic or polyatomic molecules with rich rovibrational structure—motivated by fundamental physics applications [22, 23] that include the search for particles beyond the Standard Model [24–29], fifth forces [30–32], the time variation of the electron-to-proton mass ratio [33–36], and dark matter [37, 38]. Molecules also hold promise as new platforms for quantum computation and simulation [39–48]. Recent experiments have shown quantum logic rotational spectroscopy of trapped  $\text{CaH}^+$  ions [49] and magic wavelength vibrational spectroscopy of  $\text{Sr}_2$  [50] at a precision of a few parts in  $10^{-13}$ . However, accurate vibrational spectroscopy of neutral molecules at (or below) the  $10^{-13}$  level remains difficult and unexplored [51–56].

Here, we extend the lattice clock architecture to trapped neutral molecules and characterize the systematic frequency shifts in a  $\text{Sr}_2$  vibrational lattice clock, achieving a total fractional systematic uncertainty of  $4.5 \times 10^{-14}$ , comparable to the earliest realizations of

optical atomic lattice clocks [57–59]. By carefully controlling the systematic shifts, we measure the absolute clock frequency to 13 digits, establishing it as one of the best known molecular frequencies in the terahertz (THz) band [60]. We leverage this to characterize the electronic ground potential of the strontium dimer—originating from the van der Waals bonding of two closed-shell atoms—by determining the dissociation energy of  $^{88}\text{Sr}_2$  with an accuracy surpassing the previous record for a diatomic molecule [53]. The results described here may be applied to a wide class of molecules (e.g., hydrogen isotopologues [61]), enabling the refinement of molecular quantum electrodynamics calculations, tests of fundamental laws, and potentially open new pathways for THz frequency metrology [62–64].

## II. VIBRATIONAL CLOCK

The basic scheme of the molecular clock is as follows. We operate the clock on the pure vibrational transition between the weakest bound and most tightly bound irrotational states,  $(v = 62, J = 0) \rightarrow (v = 0, J = 0)$ , in the  $X^1\Sigma_g^+$  ground potential of  $^{88}\text{Sr}_2$ . Here,  $v$  and  $J$  denote the vibrational and total angular momentum quantum numbers, respectively. In the absence of other fields, the blackbody radiation (BBR) limited lifetimes of the clock states exceed  $10^5$  years [50]. The vibrational splitting of  $\sim 32$  THz constitutes the clock frequency,  $f_{\text{clock}}$ . As a direct transition between  $J = 0$  states is strictly forbidden, we drive the clock transition via a Raman process using two diode lasers detuned from the intermediate excited state  $(1)0_u^+(v' = 11, J' = 1)$ . The relevant potentials are shown in Fig. 1(a).

The measurements take place in a one-dimensional optical lattice at 1005 nm. Trapped samples of ultracold molecules are created by photoassociating laser cooled strontium atoms at 2  $\mu\text{K}$  to the  $(1)1_u(v' = -1, J' =$

\* These authors contributed equally to this work.

† Present address: Procter and Gamble Polska Ltd., Zabraniecka 20, 03-872 Warsaw, Poland

‡ tanya.zelevinsky@columbia.edu

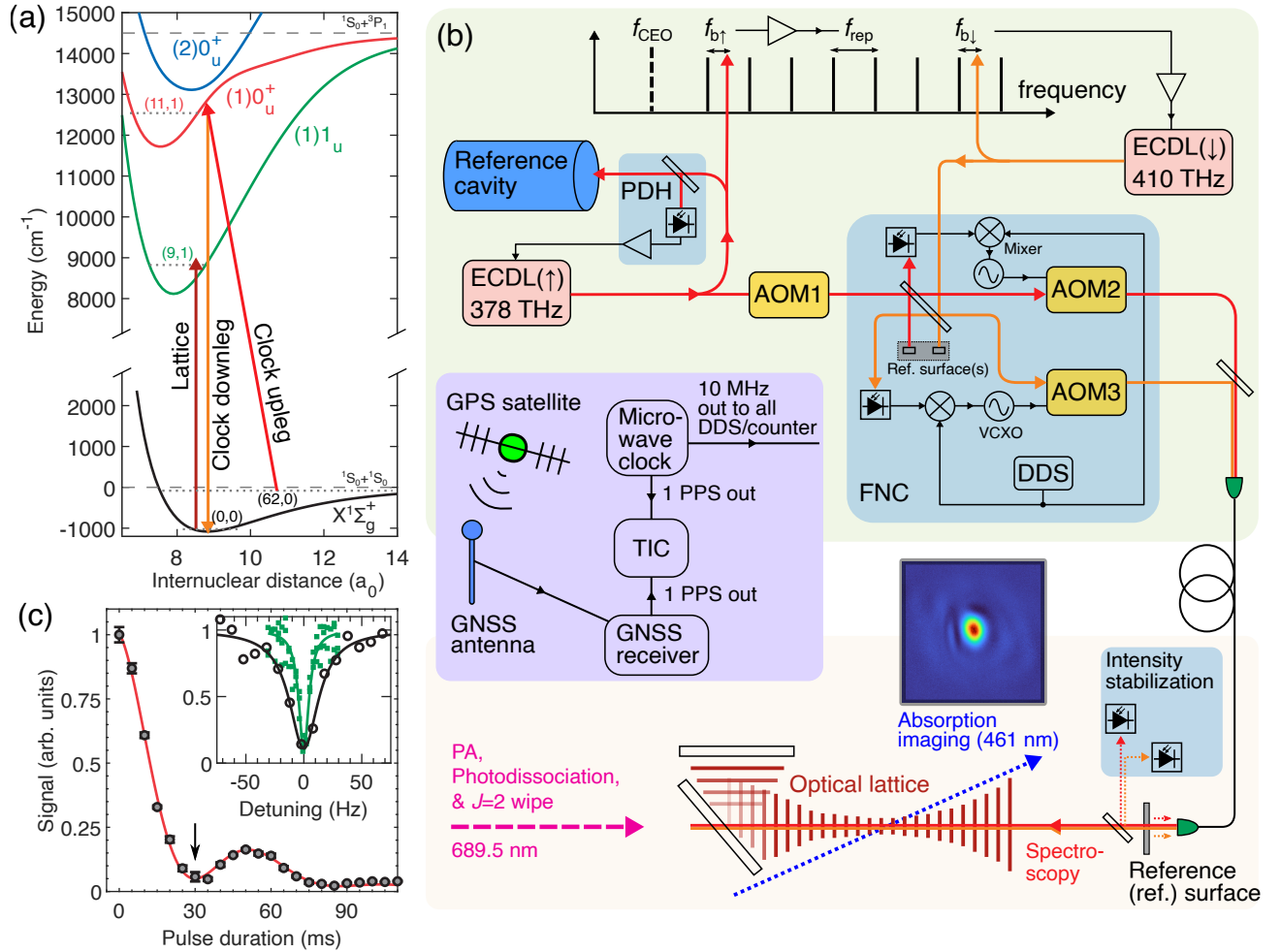


FIG. 1. Vibrational molecular lattice clock. (a) Raman lasers (upleg, red arrow; downleg, orange arrow) detuned from an intermediate state in  $(1)0_u^+$  probe the vibrational clock transition between  $(v = 62, J = 0)$  and  $(v = 0, J = 0)$  in the  $X^1\Sigma_g^+$  ground potential. The optical lattice (brown arrow) off-resonantly addresses an isolated rovibronic state in  $(1)1_u$  to induce magic trapping conditions. (b) Experimental setup. The upleg master laser is stabilized to a reference cavity using the Pound-Drever-Hall (PDH) technique, and its phase coherence is transferred to the downleg laser via a frequency comb. The molecules are held in the 1D optical lattice. Co-propagating clock lasers are delivered to the molecules via an optical fiber with active fiber noise cancellation (FNC). The spectroscopic signal derives from absorption imaging of  $X(62, 0)$  photofragments at a slight grazing angle relative to the lattice. A Rb microwave standard acts as a transfer oscillator between the molecular clock and GPS time for the absolute frequency measurement. Further information is given in the main text and Appendices A and B. (c) Two-photon Rabi oscillations between the clock states driven at the operational probe intensities (filled circles, experimental data averaged over 8 consecutive runs, error bars represent  $1\sigma$  uncertainties; solid red line, analytical fit to an exponentially decaying sinusoid). We observe lines as narrow as 11(1) Hz (inset, green squares). For clock operation, we perform Rabi spectroscopy with a 30 ms  $\pi$ -pulse duration (indicated by the black arrow), resolving 30(2) Hz linewidths consistent with the expected Fourier limit (inset, black open circles). Each point in the inset is a single shot of the experiment, and solid lines are Lorentzian fits.

1) rovibronic state. This efficiently produces  $X(62, 0)$  ground state molecules thanks to the large transition strength [65]. Molecules formed in the undesired  $J = 2$  excited rotational state are photodissociated, and the remaining atoms are wiped out of the trap with resonant 461 nm laser light. Our detection scheme relies on state-selective photofragmentation of  $X(62, 0)$  followed by absorption imaging of the slow-moving atoms. As this destroys the molecular sample, the entire sequence is iter-

ated to scan the clock transition. See Appendix A for an elaboration of the state preparation.

Raman clock spectroscopy is deeply in the Lamb-Dicke regime for co-propagating probes along the axial direction of the optical lattice (Lamb-Dicke parameter  $\eta_{\text{LD}} \lesssim 0.02$ ). The upleg (or pump) master laser at 378 THz (793 nm) is stabilized to a high finesse ultra-low expansion reference cavity with a measured drift rate of 0.03 Hz/s that is compensated using a linearly-ramped

acousto-optic modulator. The phase coherence of the upleg is transferred to the teeth of an erbium-fiber-laser-based optical frequency comb by actuating on its repetition frequency [Fig. 1(b)]. The carrier-envelope offset frequency of the comb is stabilized to a Rb standard that also serves as the laboratory timebase. The downleg (or anti-Stokes) laser at 410 THz (731 nm) is similarly phase locked to the comb to benefit from partial cancellation of laser noise, resulting in a relative frequency jitter between the up and downleg lasers that is approximately  $12\times$  smaller than the jitter of the upleg laser. The upleg is passed through an acousto-optic modulator (AOM1 in Fig. 1(b)) and the first order diffraction is used to iteratively step the difference frequency of the clock lasers across  $f_{\text{clock}}$ . The same acousto-optic modulator controls the interrogation duration by pulsing the upleg, and we leave the downleg constantly irradiating (but blocked with a mechanical shutter during the state preparation process). Both clock lasers are delivered to the molecules via the same optical fiber, but active fiber noise cancellation [66, 67] is implemented separately; see Appendix B.

Figure 1(c) shows two-photon Rabi oscillations driven by the clock lasers at the operational Rabi frequencies. Our apparatus is capable of producing clock lines with full width at half-maximum as narrow as 11(1) Hz corresponding to a  $Q$ -factor of  $2.9 \times 10^{12}$ , with no fundamental obstacles for future improvement. However, pulse durations of  $\sim 100$  ms complicate the determination of molecular densities due to single- and two-body losses [50, 65, 68]. As a compromise, we evaluate clock systematics by performing Rabi spectroscopy with a 30 ms  $\pi$ -pulse, scanning Fourier-limited peaks of 30(2) Hz. The inset to Fig. 1(c) shows a narrow spectrum as well as a typical spectrum consisting of 15 experimental iterations (taking a total duration of  $\sim 20$  s) that is fitted to a Lorentzian function to determine the line center.

### III. RESULTS

#### A. Systematic evaluation

Table I details the uncertainty budget of the molecular clock under operational conditions. Summing the uncertainties of all contributors in quadrature, we report a total systematic uncertainty of  $4.5 \times 10^{-14}$ .

We leverage the short term frequency stability of our reference cavity to average down the uncertainty of a given systematic. Most frequency corrections in Table I are determined by probing the clock transition in an interleaved fashion; i.e., we alternate an experimental parameter between two values and record the corresponding pair of line centers. This is repeated to gather statistics, and the clock shift  $\Delta f_{\text{clock}}$  is computed as a weighted average. We scale up all statistical uncertainties by the square root of the reduced chi-square statistic ( $\chi_{\text{red}}^2$ ) if  $\chi_{\text{red}}^2 > 1$ . Finally, the shift is extrapolated to determine

TABLE I. Systematic uncertainty budget for the strontium molecular clock under operating conditions. See Appendix C for the description of minor systematics not in the main text. All values are expressed in fractional units ( $\times 10^{-14}$ ).

Systematic	Correction	Uncertainty
Lattice Stark ( $E1, M1, E2$ )	100.1	3.4
Lattice Stark (hyperpolarizability)	-50.8	1.9
Probe Stark (total)	31.5	2.2
BBR	-2.2	0.4
Density	-0.6	0.3
Higher order Zeeman	0	0.2
Doppler	0	0.1
<b>Total</b>	<b>77.9</b>	<b>4.5</b>

the frequency correction for the clock at the operational parameter value.

#### 1. Lattice light shift

Magic—or state-insensitive—trapping conditions can be engineered for the vibrational clock states by off-resonantly addressing  $X^1\Sigma_g^+(0,0) \rightarrow (1)1_u(9,1)$  with the lattice. This protocol predominantly tunes the polarizability of  $X(0,0)$ , which matches that of  $X(62,0)$  at a magic detuning of 4.493(3) GHz [68]. Importantly, the neighboring  $(1)1_u(v',1)$  rovibronic resonances are spaced at intervals of  $\sim 2$  THz, and may cause deleterious shifts due to lattice light impurity (e.g., amplified spontaneous emission [69]). To mitigate this, the lattice light derives from a Ti:sapphire laser stabilized to the same optical frequency comb described in Section II. This also permits the lattice frequency,  $f_{\text{latt}} = c/\lambda_{\text{latt}}$ , to be determined with kHz-level accuracy. The light is filtered through a linear cavity (finesse of 50, and free spectral range of 2.9 GHz) before delivery to the experiment by a single-mode polarization maintaining fiber and retroreflected to form the optical lattice. A weak reflection from the vacuum window is used for lattice intensity stabilization during normal operation. The lattice polarization is linear and defines the quantization axis for the  $X^1\Sigma_g^+$  states [70].

We investigate the effect of lattice light over a range of  $f_{\text{latt}}$ . At each  $f_{\text{latt}}$  we make interleaved measurements of the clock shifts, alternating the trap depth  $U_0$  between a reference depth and four other depths spanning from  $300 E_r$  to  $1100 E_r$ , where  $E_r \equiv h^2/(2M\lambda_{\text{latt}}^2)$  is the recoil energy and  $M$  is the molecular mass. The trap depths are determined from the axial trapping frequencies (Appendix D). Small corrections ( $< 0.3 \times 10^{-14} \times f_{\text{clock}}$ ) were made to account for density shifts. As shown in Fig. 2(a), our measurements reveal nonlinear light shifts, demonstrating clear evidence for hyperpolarizability at this lattice wavelength. The origin of this effect is currently under investigation, but we hypothesize a connection with previously observed quadratic lattice scattering rates in a similar experiment [50].

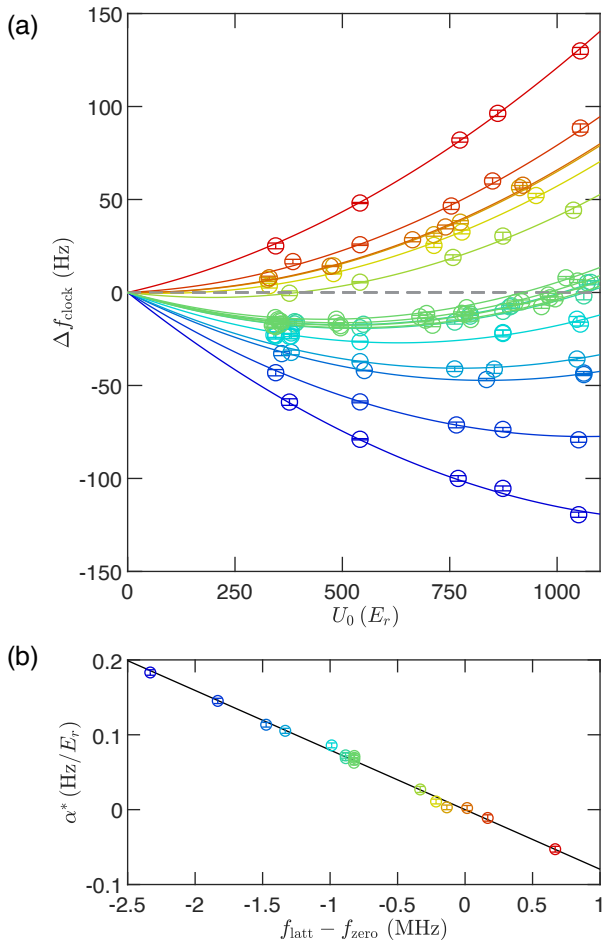


FIG. 2. (Color online) Clock shifts due to the lattice light. (a) Nonlinear shifts of the molecular clock frequency versus trap depth. For a given lattice frequency (color coded), we make interleaved measurements of clock shifts (open circles) with respect to a reference trap depth ( $\sim 500 E_r$ ), and fit the data to parabolas (solid lines) with a global quadratic parameter,  $-\beta^*$ . (b) Linear light shift coefficient,  $\alpha^*$ , versus lattice frequency (color code matches (a)), and the linear fit (black solid line).  $\alpha^*$  is predominantly due to the  $E1$  differential polarizability and is nulled at  $f_{\text{zero}}$ . By tuning  $\alpha^*$ , we can find conditions where the sensitivity of  $\Delta f_{\text{clock}}$  to fluctuations in  $U_0$  is minimal at our operational trap depth of  $487(4) E_r$  (dark green points). Error bars represent  $1\sigma$  uncertainties.

In order to characterize the lattice shifts, we adopt the thermal model described in Ref. [71],

$$\Delta f_{\text{clock}} = -\alpha^* U_0 - \beta^* U_0^2, \quad (1)$$

where  $\alpha^*$  and  $\beta^*$  are empirically obtained from parabolic fits to the measured differential shifts. These parameters are effective values dependent on the trapping conditions:  $\alpha^*$  is related to the differential electric-dipole ( $E1$ ), magnetic-dipole ( $M1$ ) and electric-quadrupole ( $E2$ ) polarizabilities, while  $\beta^*$  is related to the differential hyperpolarizability. Crucially, the polynomial form of Eq. (1) hinges on a linear scaling of the sample temperature with

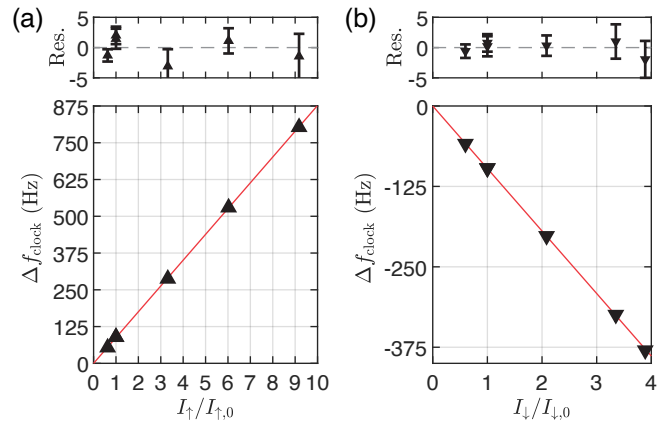


FIG. 3. Clock shifts at the operational Raman detuning as a function of (a) the upleg laser intensity, and (b) the downleg laser intensity. The horizontal axes are normalized by the respective operational intensities,  $I_{\uparrow,0}$  and  $I_{\downarrow,0}$ . Solid lines are linear fits to the data. Residuals are plotted in units of Hz. Error bars represent  $1\sigma$  uncertainties.

$U_0$ , which we verify to hold true for our molecules using Raman carrier thermometry (Appendix D). We do not expect non-polynomial terms (e.g.  $\propto \sqrt{U_0}$ ) to be significant at the level of the current evaluation.

The fits give  $\beta^* = -6.81(22) \times 10^{-5} \text{ Hz}/E_r^2$  as a global parameter. Additionally, the results for  $\alpha^*$  versus  $f_{\text{latt}}$  are shown in Fig. 2(b), and a linear fit yields a sensitivity slope  $\partial\alpha^*/\partial f_{\text{latt}} = -0.0796(16) \text{ Hz}/(\text{MHz } E_r)$  as well as an  $x$ -intercept  $f_{\text{zero}} = 298\,368\,568.844(21) \text{ MHz}$ . Operating the molecular clock at a trap depth of  $U_{\text{opt}} = 487(4) E_r$  and  $f_{\text{latt}} - f_{\text{zero}} = -0.821(21) \text{ MHz}$ , we determine the correction terms to be  $\alpha^* U_{\text{opt}} = 31.8(1.1) \text{ Hz}$  and  $\beta^* U_{\text{opt}}^2 = -16.2(6) \text{ Hz}$ , summing to a fractional correction of  $49.3(3.8) \times 10^{-14}$ . Under these conditions,  $\Delta f_{\text{clock}}$  is first-order insensitive to changes in  $U_0$  (dark green points in Fig. 2).

## 2. Probe light shift

Probe light shifts pose an inherent challenge for two-photon spectroscopy. This is even more so for scalar clock states ( $J=0$ ) that preclude the use of laser polarization-based cancellation schemes [72]. Here, the clock shifts scale linearly as the probe intensities are low, and are related to the differential polarizability at the respective probe wavelength ( $\lambda_p$ ),

$$\Delta f_{\text{clock}} = \frac{I_p}{2h\epsilon_0 c} [\alpha_0(\lambda_p) - \alpha_{62}(\lambda_p)], \quad (2)$$

where  $\alpha_v$  is the  $E1$  polarizability for the vibrational state  $v$ ,  $I_p$  is the probe laser intensity, and  $p \in \{\uparrow, \downarrow\}$  specifies the laser: upleg ( $\uparrow$ ) or downleg ( $\downarrow$ ). Figure 3 shows that linear extrapolation of probe shifts suffices for a molecular clock at the few  $10^{-14}$  level.

While tailored pulse sequences to alleviate probe light shifts have been proposed [73–76], for this evaluation we opted for a more straightforward strategy. We can minimize the total probe light shift by using so-called balanced intensity ratios satisfying the condition  $I_{\uparrow}[\alpha_0(\lambda_{\uparrow}) - \alpha_{62}(\lambda_{\uparrow})] = -I_{\downarrow}[\alpha_0(\lambda_{\downarrow}) - \alpha_{62}(\lambda_{\downarrow})]$ . At the same time, a large Raman detuning—relative to the intermediate  $(1)0_u^+(11,1)$  excited state—is preferred so that off-resonant scattering from the probes have a negligible effect on the accessible coherence times. Figure 3 demonstrates that such conditions exist in our clock for blue detunings where the baseline polarizability differences at the probe wavelengths have opposite signs, in agreement with our polarizability model (Appendix E). We operate at a Raman detuning of +14.973 GHz, much greater than the 5 MHz natural linewidth of the intermediate state [68].

We evaluate  $\Delta f_{\text{clock}}$  for each leg separately. Using a motorized neutral density filter, we switch between two intensity values for one leg while keeping that of the other leg constant at its operational value. The  $\pi$ -pulse durations are adjusted accordingly. Typical settings for the interleaved measurements are  $(P_{\uparrow,0}, 9P_{\uparrow,0})$ , and  $(P_{\downarrow,0}, 3.5P_{\downarrow,0})$  where  $P_{p,0} = I_{p,0}(\pi w_p^2/2)$  are the operational powers measured with a calibrated power meter immediately before the vacuum window. These shifts are scaled by the measurement lever arms to obtain the clock corrections at the operational settings:  $-(\Delta f_{\text{clock}}/\Delta P_p) \times P_{p,0}$ . We find the corrections to be  $-277.5(1.4) \times 10^{-14}$  for the upleg, and  $309.0(1.7) \times 10^{-14}$  for the downleg. Drifts in  $\Delta P_p$  are at the sub-percent level over the  $\sim 2000$  s duration for each probe light shift evaluation, and the weighted averages of  $f_{\text{clock}}$  typically have  $\chi_{\text{red}}^2 \sim 1$ . Accurate knowledge of the beam waists  $w_p$  is not necessary as they are robust during an evaluation, and are common factors that drop out in calculations. Long-term drifts due to beam pointing instability may be monitored and countered by benchmarking the probe intensities using the molecules (e.g., through an Autler-Townes splitting, an on-resonance scattering rate, or the two-photon Rabi oscillation frequency), which we leave to future work.

### 3. Blackbody radiation shift

Homomuclear dimers are infrared inactive, conferring natural immunity to blackbody radiation (BBR). Using the formulas derived in Ref. [77], the frequency correction due to BBR is calculated to be  $-0.70(14)$  Hz at an operating chamber temperature of  $T_{\text{c,o}} = 302(1)$  K; see Appendix F for a description of the chamber thermometry. The uncertainty is dominated by *ab initio* calculations of the dc polarizabilities of the clock states (Appendix E). Comparison with experimentally measured ac polarizability ratios show agreement at the level of 10–20%, to be expected from typical accuracies of theoretical transition strengths. Therefore, we assign a conservative

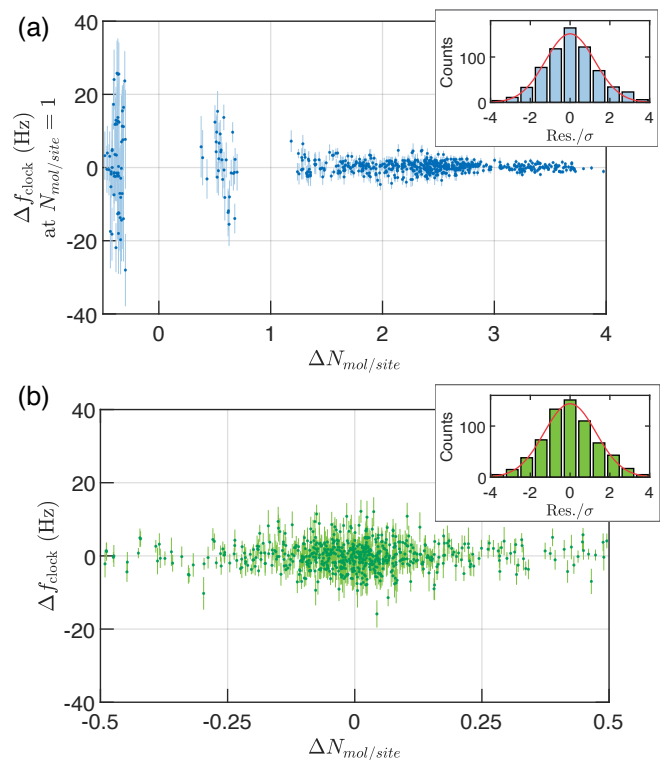


FIG. 4. Density shift evaluation. (a) Clock shifts due to molecular collisions extrapolated to operating conditions (1 molecule per lattice site, averaged over filled sites), plotted versus the change in molecule number per site used for the interleaved measurement. A single constant suffices to fit the data ( $0.20(10)$  Hz,  $\chi_{\text{red}}^2 = 1.7$ ). (b) In the same dataset, the shift between successive resonances taken under identical experimental settings serves as a control experiment to check for technical offsets. As expected, this averages to zero ( $0.03(20)$  Hz,  $\chi_{\text{red}}^2 = 2.0$ ). All statistical errors are scaled up by  $\sqrt{\chi_{\text{red}}^2}$ . Error bars represent  $1\sigma$  uncertainties. Both insets show the histogram of normalized residuals, and the solid red lines are Gaussian fits.

fractional uncertainty of 20% for the BBR shift.

### 4. Density shift

Our  $^{88}\text{Sr}_2$  molecules are unprotected against *s*-wave collisions due to their bosonic character. The one-dimensional lattice forms a series of microtraps, each with a trap volume proportional to  $(T/\bar{\omega}^2)^{3/2}$ . Here,  $T$  is the temperature of the molecules, and  $\bar{\omega}$  is the geometric mean of the angular trapping frequencies. We investigate density dependent shifts arising from dimer-dimer collisions by modulating the average number of molecules per lattice site ( $N_{\text{mol/site}}$ ) at the beginning of the clock pulse. This is achieved by inserting a wait time immediately after photoassociation (PA) so that two-body collisions naturally reduce the molecule number [65, 68]. Fluctuations in  $N_{\text{mol/site}}$  are typically  $< 20\%$ , and we assume

equal occupancy across filled sites. Since both  $T$  and  $\bar{\omega}^2$  scale similarly with  $U_0$ , and the lattice intensity is stabilized,  $N_{\text{mol/site}}$  is a robust observable proportional to the molecular density.

Assuming linear density shifts, we scale our differential measurements to find  $\Delta f_{\text{clock}}$  at the normal operating value of  $N_{\text{mol/site}} = 1$ . Figure 4(a) summarizes the measurements performed at various number differences ( $\Delta N_{\text{mol/site}}$ ) suggesting a correction of  $-0.20(10)$  Hz, or  $-0.63(31) \times 10^{-14}$  in fractional units, due to collisional shifts. Control measurements using spectra taken under common experimental settings do not show evidence of spurious offsets in our data [Fig. 4(b)]. It is instructive to compare the magnitude of our density shift with similarly performing atomic clocks. From a trap calibration (Appendix D) we estimate a shift coefficient of  $8(4) \times 10^{-25} \text{ cm}^3$  after normalizing by the transition frequency. This is rather similar to the analogous optical atomic clock with bosonic  $^{88}\text{Sr}$  ( $\sim 2 \times 10^{-25} \text{ cm}^3$  [78]), while being orders of magnitude smaller than in Cs ( $\sim 1 \times 10^{-21} \text{ cm}^3$  [79, 80]) or Rb microwave clocks ( $\sim 5 \times 10^{-23} \text{ cm}^3$  [81]). Future work may circumvent collisional shifts altogether by preparing samples with single molecule occupancy in a three-dimensional lattice [82–85] or an optical tweezer array [40, 86–88].

## B. Absolute frequency evaluation

As illustrated in Fig. 1(b), we reference all RF frequency counters and direct digital frequency synthesizers (DDS) in the experiment to a free-running Rb microwave standard (our local timebase). Calibration of this Rb clock is accomplished by comparing its 1 pulse-per-second (PPS) output with that of a dual-band global navigation satellite system (GNSS) receiver on a time interval counter (TIC). The Rb clock, therefore, serves as a transfer oscillator between the molecular clock and Global Positioning System (GPS) time. Occasionally, we manually aligned the Rb clock frequency relative to GPS during periods of experimental downtime if it exceeded a fractional offset of  $1 \times 10^{-11}$  (but not during a measurement trial or TIC log).

Each measurement trial of the absolute clock frequency is performed under operational conditions, where the molecular clock systematics are controlled at the level quoted in Table I. We repeatedly scan the clock transition to obtain a time series of the line centers, while simultaneously counting the repetition rate of the frequency comb. The probe light shifts were evaluated every trial to account for potential daily variations in probe laser beam pointing. We log the TIC measurements continuously for at least 24 hours to average the satellite link, longer than the uptime of the molecular clock. The TIC measurements as a function of elapsed time are split into 6 segments, to which independent linear fits were made. We take the average (standard deviation) of the slopes of the linear fits to be the fractional frequency offset (un-

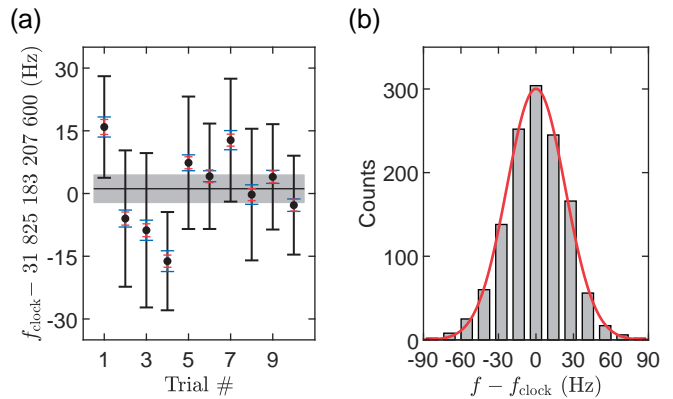


FIG. 5. (a) Absolute frequency of the clock transition measured over 10 trials (filled black circles) with all known frequency offsets corrected, including that of the local timebase (see main text for details). Blue error bars are  $1\sigma$  statistical uncertainties, dominated by the determination of the comb repetition rate rather than the stability of the scanned molecular clock lines. Red error bars are  $1\sigma$  systematic uncertainties due to the molecular clock only (see Table I). Black error bars are  $1\sigma$  total uncertainties, where the uncertainties of the local timebase calibrations are added in quadrature with the statistical and molecular clock systematic uncertainties. The black horizontal line shows the weighted average, and the shaded grey area shows the associated  $\pm 1\sigma$  standard error of the mean ( $\chi_{\text{red}}^2 = 0.57$ ). (b) Histogram of all clock frequency measurements in the 10 trials, relative to the weighted average of  $f_{\text{clock}}$ . The solid red line is a Gaussian fit to the histogram.

certainty) of the Rb clock relative to GPS. Since each TIC measurement is started by the rising edge of the 1 PPS from the Rb clock and stopped by the rising edge of the 1 PPS from the GNSS receiver, an average positive (negative) slope implies that a positive (negative) correction has to be made to the uncalibrated molecular clock frequency.

Figure 5 shows the results of the measurement campaign, consisting of 10 trials performed on separate days. A weighted average yields the absolute frequency of the  $^{88}\text{Sr}_2$  vibrational clock to be  $f_{\text{clock}} = 31\,825\,183\,207\,601.1(3.3)$  Hz, with a fractional uncertainty of  $1.0 \times 10^{-13}$  limited by the drift of the Rb standard during its calibration. The scale intervals of GPS time and International Atomic Time (TAI) differed by a few parts in  $10^{-15}$  during the campaign [89].

## IV. CONCLUSION

Few frequency standards currently exist in the THz band [60]. Our molecular clock serves as a THz reference and can generate stable radiation at  $9.4 \mu\text{m}$  via photomixing [90, 91]. Alternatively, transitions in heteronuclear isotopologues could be driven directly with quantum cascade lasers [92, 93]. To our knowledge,  $f_{\text{clock}}$  represents one of the most accurately measured molecu-

lar frequencies to date, on par with the unidentified rovibrational interval in  $\text{OsO}_4$  near the  $R(10) (00^0_1)-(10^0_0)$  emission line of the  $^{12}\text{C}^{16}\text{O}_2$  laser. This absorption line in  $\text{OsO}_4$  is a secondary representation of the SI second [60], and was compared directly against a primary cesium standard by stabilizing a  $\text{CO}_2$  laser to the specific saturated absorption feature of  $\text{OsO}_4$  in a high-finesse cavity [94, 95]. We expect to reduce the uncertainty of our local timebase calibration to the same level as the molecular clock systematics (or better) by upgrading to a standard with intrinsically lower instability and utilizing two-way time transfer schemes.

Molecular spectroscopy is increasingly appreciated as a fertile ground in the search for new physics. The reported Hz-level molecular clock is a starting point for elucidating the bonding of the  $\text{Sr}_2$  dimer across a large range of internuclear distances and investigating hypothesized hadron-hadron interactions for differing nucleon numbers [31]. The sum of  $f_{\text{clock}}$  with the binding energy of the least bound state  $X(62, 0)$  yields the dissociation energy ( $D_0$ ) of our molecule with respect to the  $^1S_0 + ^1S_0$  threshold. While the analogous least bound vibrational states of  $^{84}\text{Sr}_2$  and  $^{86}\text{Sr}_2$  are known with sub-kHz uncertainties [96, 97], the current best measurement for  $^{88}\text{Sr}_2$  is at the kHz-level [98]. Nevertheless, taking the binding energy of  $X(62, 0)$  to be 136.6447(50) MHz from Ref. [98], which was determined using two-photon dissociation, we find  $D_0(^{88}\text{Sr}_2) = 31\,825\,319\,852(5)$  kHz, or  $1\,061.578\,402\,09(17)$   $\text{cm}^{-1}$ . This is an improvement by 5 orders of magnitude over the previously reported value for  $\text{Sr}_2$  in available literature [99], and sets a new accuracy record for the determination of a molecular dissociation energy ( $1.6 \times 10^{-10}$  fractional uncertainty). To list a few competitive results, dissociation energies have been reported with fractional uncertainties of  $4.4 \times 10^{-10}$  for  $^{87}\text{Rb}^{133}\text{Cs}$  [53],  $6.9 \times 10^{-10}$  for ortho- $\text{H}_2$  [54],  $8.6 \times 10^{-10}$  for para- $\text{H}_2$  [55], and  $7.1 \times 10^{-10}$  for ortho- $\text{D}_2$  [56].

In summary, we have demonstrated a vibrational molecular clock with a total systematic uncertainty of  $4.5 \times 10^{-14}$ , entering a new domain in high resolution molecular spectroscopy. Our results are enabled by merging the key strengths of atomic clock techniques with molecular quantum science. Implementation of deeper atomic cooling [100, 101], operation at lower lattice and probe laser intensities, strengthening of the overall optomechanical stability, and other strategies for accessing longer coherence times should realistically improve the systematic uncertainty and facilitate its evaluation.

## ACKNOWLEDGMENTS

We gratefully thank J. Sherman for insightful discussions and invaluable advice on the absolute frequency measurement, and V. Lochab for early contributions to the vacuum chamber thermometry. This work was supported by NSF grant PHY-1911959, AFOSR MURI FA9550-21-1-0069, ONR grant N00014-21-1-2644, a Cen-

ter for Fundamental Physics grant from the John Templeton Foundation & Northwestern University, the Brown Science Foundation, and the Polish National Science Centre (NCN) grant 2016/20/W/ST4/00314. M. B. was partially funded by the Polish National Agency for Academic Exchange within the Bekker Programme, project PPN/BEK/2020/1/00306/U/00001, and by NCN, grant 2017/25/B/ST4/01486.

## Appendix A: State preparation

Our experiments start with a thermal beam of  $^{88}\text{Sr}$  atoms decelerated by a Zeeman slower and laser cooled in a first-stage (blue) magneto-optical trap (MOT) using the  $^1S_0 \rightarrow ^1P_1$  transition at 461 nm. We employ repumpers on the  $^3P_2 \rightarrow ^3S_1$  and  $^3P_0 \rightarrow ^3S_1$  transitions at 707 nm and 679 nm respectively. A second-stage (red) MOT on the narrower  $^1S_0 \rightarrow ^3P_1$  intercombination at 689 nm further cools the atoms to a typical temperature of 2  $\mu\text{K}$ . Throughout the cooling sequence ( $\sim 500$  ms), a one-dimensional optical lattice at 1005 nm overlaps with the atom cloud, and atoms with kinetic energies lower than the trap depth are loaded into the lattice. The surrounding magnetic field is lowered to  $< 0.6$  G to prepare for molecule production and spectroscopy. The lattice is formed by retroreflecting the lattice laser beam and, in this study, oriented horizontally with respect to gravity due to practical limitations.

Spin statistics and molecular symmetry imply that only even values of total angular momentum  $J$  exist for ground state  $^{88}\text{Sr}_2$  molecules. While rotational factors favor the decay from  $1_u(J' = 1)$  to  $X(J = 0)$ , a finite number of  $X(J = 2)$  molecules still form. Thus, to purify the gas we photodissociate the  $X(62, 2)$  molecules 30 MHz above the  $^1S_0 + ^3P_1$  threshold, imparting more than sufficient kinetic energy to guarantee these photofragments leave the trap. We do this concurrently with photoassociation (PA) by adding a frequency sideband to the PA laser with an acousto-optic modulator. We use PA pulse durations of  $\sim 2$  ms. The remaining atoms are blasted out of the trap with resonant 461 nm laser light. For the operational trap depth in this study, we prepare  $6 \times 10^3$  molecules in the initial clock state  $X(62, 0)$ , spread across approximately 520 lattice sites. To mitigate density shifts during clock operation, we further hold the molecules for a short duration ( $\sim 150$  ms) leveraging on the natural two-body inelastic collisions to reduce lattice occupancy to 1 molecule per site, averaged over filled lattice sites. Finally, photodissociation of  $X(62, 0)$  near the  $^1S_0 + ^3P_1$  threshold produces slow moving atoms that we absorption image to use as our spectroscopic signal [Fig. 1(b)]. Mechanical shutters provide secondary shuttering of all laser beams (except the lattice) prior to entering the vacuum chamber, in addition to the fast primary shuttering performed using acousto-optic modulators. In this manner, we ensure that the molecules interact only with the Raman clock lasers and the lattice during clock interro-

gation. A complete account of our molecule production or detection methods are described in Refs. [102, 103].

### Appendix B: Raman clock lasers

Our reference cavity is formed from two fused silica mirrors bonded to an ultra-low expansion glass spacer placed in a vacuum housing maintained at the measured zero-crossing temperature for the coefficient of thermal expansion. The cavity finesse is  $> 3 \times 10^5$  from ring-down measurements. The upleg diode laser also serves as the master laser, and is stabilized to the cavity using the Pound-Drever Hall technique. We phase lock the repetition rate of an erbium-fiber-laser-based optical frequency comb directly to the upleg. Observations of the counted repetition rate for over a month prior to the campaign reveal a cavity drift rate of 0.03 Hz/s, which we compensate using an acousto-optic modulator in the optical path of the master laser to the cavity. The frequency synthesizer that performs this linear compensation updates every second. By phase locking the downleg diode laser directly to the comb, the comb thus acts as a transfer oscillator. To suppress common-mode phase fluctuations, the beats of the clock lasers with the comb are chosen to have the same sign and frequency; i.e.,  $f_{b\uparrow} = f_{b\downarrow}$  in Fig. 1(b).

The clock lasers are injected into the same polarization maintaining single-mode fiber and delivered to the adjacent optical table where the experiments take place. Since the wavelengths are sufficiently different that the laser beams may sample non-identical paths in a given refractive medium, active fiber noise cancellation [66] on each clock leg is implemented using independent phase actuators (acousto-optic modulators AOM2 and AOM3 in Fig. 1(b)). The voltage-controlled crystal oscillators (VCXO) provide identical RF frequencies to AOM2 and AOM3, and are phase locked to the same RF reference from a direct digital frequency synthesizer (DDS). The phase reference surface at the experiment table is a single partially reflecting mirror, while the surfaces on the laser table are mounted on a common rigid pedestal post with the clock lasers approaching the surfaces in the same direction. To minimize the number of optical elements and unstabilized path lengths, the clock lasers interrogate the molecules from the opposite direction as the PA and photodissociation lasers. The total uncompensated path in air is approximately 50 cm. The polarizations of the probes are identical, linear, and parallel to the small applied magnetic field, but perpendicular relative to that of the lattice in this work. During the state preparation sequence described in Appendix A, both clock lasers are blocked by a mechanical shutter before the beams enter the vacuum chamber.

### Appendix C: Other clock systematics

The use of  $J = 0$  clock states and the lack of hyperfine structure confer several advantages. Firstly, this affords a high degree of insensitivity to external magnetic fields [104]. Nevertheless, higher order processes may introduce a clock shift through the Raman intermediate  $0_u^+(J' = 1)$  state, and the  $1_u(J' = 1)$  state off resonantly addressed by the magic lattice. To investigate this possibility, we experimentally vary the applied magnetic field during clock interrogation by 3.2 G, and interleaved measurements suggest a differential shift of 0.08(29) Hz. Extrapolating to the magnetic field during normal running conditions in this paper, this is consistent with a null value with a fractional uncertainty of  $2 \times 10^{-15}$ . Secondly,  $J = 0$  states are robust against laser polarization effects. However, depending on the physical origin of the differential hyperpolarizability at the lattice wavelength and the extent of mixed quantization [70], angular momentum selection rules may allow the differential hyperpolarizability to be controlled by the degree of circular polarization of the lattice laser, which we leave to future work.

First order Doppler shifts result from the relative motion of the lattice anti-nodes and the phases of the probe lasers. For example, this may be due to the mechanical motion of the lattice retroreflector, or phase chirps arising from the pulsing of an acousto-optic modulator that diffracts a probe beam. A common solution in lattice clocks is to perform fiber noise cancellation of the probe(s) using the lattice retroreflector either as the phase reference surface or as a rigid support for a separate surface, which we will implement in future work. Such shifts, if uncompensated, have been reported to be as large as  $10^{-16}$  in a Yb optical lattice clock [11]. Since the upleg is pulsed by an acousto-optic modulator, we expect these shifts to be of a similar magnitude in absolute frequency. For our transition frequency ( $\sim 32$  THz), we estimate first order Doppler shifts to be at the low  $10^{-15}$  level. The second order Doppler shift is  $< 10^{-19}$  for the typical thermal speed of our molecule.

We fit parabolas to the measured clock shifts for the lattice light shift evaluation to account for the observed hyperpolarizability effect. Given our trap parameters and the linear scaling of sample temperatures with trap depth, the polynomial fit is a reasonable approximation, and the  $M1$ - $E2$  shifts (that microscopically scale as  $\sqrt{U_0}$ ) are included in the  $\alpha^*$  effective parameter [11, 13, 71].  $M1$  and  $E2$  transitions are typically weaker than  $E1$  transitions by a factor of  $1/\alpha_{fs} \approx 137$ , where  $\alpha_{fs}$  is the fine structure constant. Moreover, the vibrational clock states have similar polarizabilities as they possess the same electronic state. As such, we do not expect higher order corrections to be relevant for the current evaluation at the  $10^{-14}$  level. In future work, calculating the differential  $M1$  and  $E2$  polarizabilities would help quantify the error associated with the thermal model.

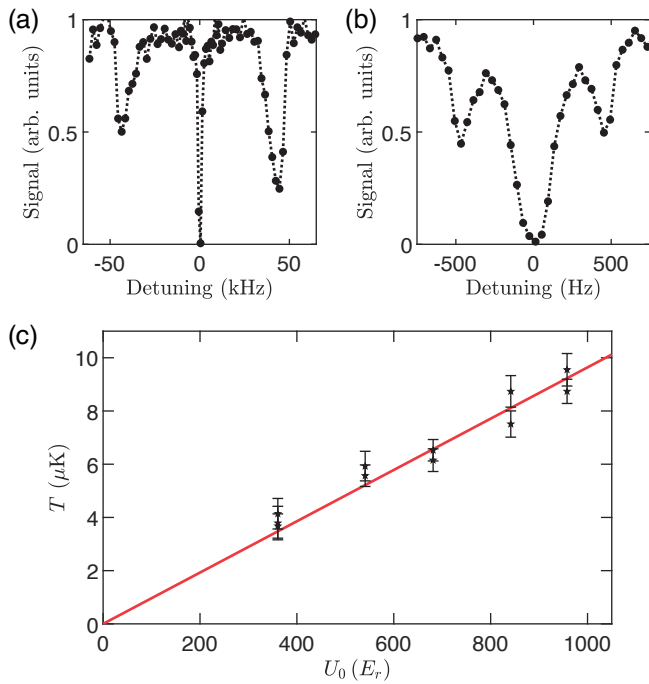


FIG. 6. Exemplary spectra of molecular (a) axial and (b) radial sidebands excited using Raman clock transitions, from which the motional frequencies are extracted to calibrate the lattice trap. (c) Measurement of the molecular temperature as a function of trap depth (black stars), done using Raman carrier thermometry. Error bars denote  $1\sigma$  uncertainties. A linear fit (red solid line) with the intercept fixed at the origin describes the data well ( $\chi_{\text{red}}^2 = 0.92$ ).

#### Appendix D: Trap calibration and Raman carrier thermometry

The axial ( $f_{\text{ax}}$ ) and radial ( $f_{\text{rad}}$ ) trap frequencies for the molecules are measured with resolved-sideband spectroscopy at the operational magic lattice wavelength [Figs. 6(a,b)]. To enhance the transition rates for the axial sidebands, we use counter-propagating probes to interrogate the naturally nearly-magic Raman transition between the adjacently bound vibrational states  $X(62,0) \rightarrow X(61,0)$ . To excite the radial sidebands, we use the Raman clock transition  $X(62,0) \rightarrow X(0,0)$  but intentionally introduce a small relative misalignment in the probe beams. The trap depths are calculated using  $U_0 = M\lambda^2 f_{\text{ax}}^2/2$ . We note that  $U_0/E_r = M^2\lambda_{\text{latt}}^4 f_{\text{ax}}^2/h^2$ , so given the same trap frequencies and  $\lambda_{\text{latt}}$ ,  $U_0/E_r$  is  $4\times$  larger for  $\text{Sr}_2$  molecules than Sr atoms. Assuming a Boltzmann thermal distribution, the trap volumes are calculated as  $V = (4\pi k_B T/\bar{\omega}^2 M)^{3/2}$ , where  $\bar{\omega} \equiv 2\pi(f_{\text{ax}}f_{\text{rad}}^2)^{1/3}$  and  $M$  is the molecular mass.

To determine  $T$ , we perform Raman carrier thermometry [68, 105] with co-propagating probes scanning  $X(62,0) \rightarrow X(0,0)$  at a non-magic wavelength (tuned  $>0.3$  THz away from the operational magic wavelength to maximize the polarizability difference). As shown in

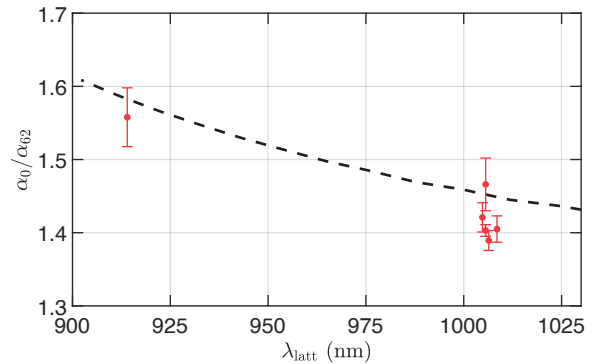


FIG. 7. The baseline ac polarizability ratio of the clock states in this study ( $\alpha_0/\alpha_{62}$ ) at various trap laser wavelengths. Red circles are experimental measurements. The black dotted line is the theory calculation.  $X \rightarrow (1)1_u$  resonances are excluded from this plot, but are included in the calculation. Error bars represent  $1\sigma$  statistical uncertainties.

Fig. 6(c), the dependence of  $T$  against  $U_0$  is well described by a linear fit to the data.

#### Appendix E: Clock state polarizabilities and BBR shifts

The electric dipole ( $E1$ ) polarizabilities of vibrational states in the  $X^1\Sigma_g^+$  potential are calculated using the sum-over-states approach [106]. For states with total angular momentum  $J = 0$ , the polarizability is a scalar quantity independent of the polarization of the electromagnetic field. Let  $|i\rangle$  represent the rovibronic wavefunction of  $X^1\Sigma_g^+(v, J = 0)$  and  $|f\rangle$  represent the rovibronic wavefunction of a state that is  $E1$ -allowed from  $|i\rangle$ . The polarizability of a molecule in  $X^1\Sigma_g^+(v, J = 0)$  is

$$\alpha_v(\omega) = \frac{1}{\hbar} \sum_f |\langle f|d_0|i\rangle|^2 \frac{2\omega_{fi}}{\omega_{fi}^2 - \omega^2}. \quad (\text{E1})$$

Here,  $d_0$  is the component of the electric dipole moment operator parallel to the lab-frame quantization ( $Z$ ) axis,  $\omega_{fi}$  is the angular frequency of the rovibronic transition, and  $\omega$  is the angular frequency of the electromagnetic field. The dc (static) polarizability is recovered for  $\omega = 0$ .

The sum in Eq. (E1) is evaluated for bound-to-bound transitions to singlet ungerade excited potentials and bound-to-continuum transitions by discretizing the continuum. We include contributions from the  $^1\Sigma_u^+$  potentials correlating to  $^1S + ^1P$  and  $^1S + ^1D$ , as well as the  $^1\Pi_u$  potentials correlating to  $^1S + ^1P$ ,  $^1S + ^1D$ ,  $^3P + ^3P$  and  $^3P + ^3D$ . The  $(1)^1\Sigma_u^+$  potential is taken from the *ab initio* calculation in Ref. [107], while the doubly-excited  $(3)^1\Pi_u$  and  $(4)^1\Pi_u$  potentials were calculated using the multireference configuration interaction method (MRCI) with the MOLPRO package [108]. The remaining potentials (including  $X^1\Sigma_g^+$ ) are empirical [99, 109]. We omit

spin-orbit and non-adiabatic couplings between the potentials. The inclusion of further high lying potentials do not change the convergence of our results.

Laser wavelengths in the range 800–1200 nm can drive transitions from  $X^1\Sigma_g^+$  to the short range part of  $(1)1_u$ . These singlet-triplet transitions are relatively weaker than singlet-singlet ones, but become important if the laser is tuned near a resonance; e.g., in the case of a magic wavelength optical trap. To properly account for these situations, we additionally include the Morse/Long-range potential of  $(1)1_u$  from Ref. [65] in the polarizability sum. Figure 7 shows the experimentally measured ac polarizability ratio  $\alpha_0/\alpha_{62}$  over a range of wavelengths, determined using a frequency-only method [65, 68], along with the calculation using Eq. (E1) showing consistency within  $< 20\%$ .

To calculate the BBR shift, we use the formulas derived in Ref. [77] and properly adapt them for molecular states. In Ref. [77], approximations were made to express the BBR shift in terms of the dc polarizability and a power series in  $k_B T_{c,o}/(\hbar\omega_{fi})$ . These approximations are also valid for our case since  $\omega_{fi}/(2\pi c) > 8000 \text{ cm}^{-1}$ , corresponding to characteristic temperatures of  $> 11500 \text{ K}$  much greater than  $T_{c,o}$ . The so-called dynamic term contributes less than 0.5% to the total BBR shift. The

correction to the vibrational clock frequency at  $T_{c,o} = 302(1) \text{ K}$  is calculated to be  $-0.70(14) \text{ Hz}$ . We quote a conservative fractional uncertainty of 20% based on the level of consistency between the measured and calculated ac polarizabilities [Fig. 7].

## Appendix F: Vacuum chamber thermometry

At the present level of precision, it is enough to estimate the temperature environment of the molecules using four negative temperature coefficient (NTC) thermistors affixed to the exterior of the vacuum chamber. The largest temperature gradient lies along the axis of the Zeeman slower, where a sapphire vacuum window facing the beam source is heated to 430 K to reduce the deposition rate by the hot atomic flux. The largest (smallest) sensor reading along this direction is  $T_{c,\max}$  ( $T_{c,\min}$ ). We model the temperature gradient as a rectangular distribution [110] and estimate  $T_{c,o} = (T_{c,\max} + T_{c,\min})/2$ , with an uncertainty of  $(T_{c,\max} - T_{c,\min})/\sqrt{12}$ . The line of sight from the molecules to the hot oven is blocked using an in-vacuum mechanical shutter during normal operation and contributes a negligible frequency shift.

- 
- [1] S. Chu, L. Hollberg, J. E. Bjorkholm, A. Cable, and A. Ashkin, Three-dimensional viscous confinement and cooling of atoms by resonance radiation pressure, *Phys. Rev. Lett.* **55**, 48 (1985).
- [2] A. Aspect, E. Arimondo, R. Kaiser, N. Vansteenkiste, and C. Cohen-Tannoudji, Laser cooling below the one-photon recoil energy by velocity-selective coherent population trapping, *Phys. Rev. Lett.* **61**, 826 (1988).
- [3] P. D. Lett, R. N. Watts, C. I. Westbrook, W. D. Phillips, P. L. Gould, and H. J. Metcalf, Observation of atoms laser cooled below the Doppler limit, *Phys. Rev. Lett.* **61**, 169 (1988).
- [4] A. Ashkin, Acceleration and trapping of particles by radiation pressure, *Phys. Rev. Lett.* **24**, 156 (1970).
- [5] A. Ashkin, Trapping of atoms by resonance radiation pressure, *Phys. Rev. Lett.* **40**, 729 (1978).
- [6] H. Katori, M. Takamoto, V. Pal'Chikov, and V. Ovsiannikov, Ultrastable optical clock with neutral atoms in an engineered light shift trap, *Phys. Rev. Lett.* **91**, 173005 (2003).
- [7] T. Bothwell, C. J. Kennedy, A. Aeppli, D. Kedar, J. M. Robinson, E. Oelker, A. Staron, and J. Ye, Resolving the gravitational redshift across a millimetre-scale atomic sample, *Nature* **602**, 420 (2022).
- [8] X. Zheng, J. Dolde, V. Lochab, B. N. Merriman, H. Li, and S. Kolkowitz, Differential clock comparisons with a multiplexed optical lattice clock, *Nature* **602**, 425 (2022).
- [9] E. Oelker, R. Hutson, C. Kennedy, L. Sonderhouse, T. Bothwell, A. Goban, D. Kedar, C. Sanner, J. Robinson, G. Marti, *et al.*, Demonstration of  $4.8 \times 10^{-17}$  stability at 1 s for two independent optical clocks, *Nat. Photon* **13**, 714 (2019).
- [10] M. Schioppo, R. C. Brown, W. F. McGrew, N. Hinkley, R. J. Fasano, K. Bely, T. Yoon, G. Milani, D. Nicolodi, J. Sherman, *et al.*, Ultrastable optical clock with two cold-atom ensembles, *Nat. Photon* **11**, 48 (2017).
- [11] W. McGrew, X. Zhang, R. Fasano, S. Schäffer, K. Bely, D. Nicolodi, R. Brown, N. Hinkley, G. Milani, M. Schioppo, *et al.*, Atomic clock performance enabling geodesy below the centimetre level, *Nature* **564**, 87 (2018).
- [12] B. Bloom, T. Nicholson, J. Williams, S. Campbell, M. Bishof, X. Zhang, W. Zhang, S. Bromley, and J. Ye, An optical lattice clock with accuracy and stability at the  $10^{-18}$  level, *Nature* **506**, 71 (2014).
- [13] T. Bothwell, D. Kedar, E. Oelker, J. M. Robinson, S. L. Bromley, W. L. Tew, J. Ye, and C. J. Kennedy, JILA SrI optical lattice clock with uncertainty of  $2.0 \times 10^{-18}$ , *Metrologia* **56**, 065004 (2019).
- [14] T. L. Nicholson, S. Campbell, R. Hutson, G. E. Marti, B. Bloom, R. L. McNally, W. Zhang, M. Barrett, M. S. Safronova, G. Strouse, *et al.*, Systematic evaluation of an atomic clock at  $2 \times 10^{-18}$  total uncertainty, *Nat. Commun.* **6**, 1 (2015).
- [15] R. Hobson, W. Bowden, A. Vianello, A. Silva, C. F. Baynham, H. S. Margolis, P. E. Baird, P. Gill, and I. R. Hill, A strontium optical lattice clock with  $1 \times 10^{-17}$  uncertainty and measurement of its absolute frequency, *Metrologia* **57**, 065026 (2020).
- [16] N. Nemitz, T. Ohkubo, M. Takamoto, I. Ushijima, M. Das, N. Ohmae, and H. Katori, Frequency ratio of Yb and Sr clocks with  $5 \times 10^{-17}$  uncertainty at 150 seconds averaging time, *Nat. Photon* **10**, 258 (2016).

- [17] K. Yamanaka, N. Ohmae, I. Ushijima, M. Takamoto, and H. Katori, Frequency ratio of  $^{199}\text{Hg}$  and  $^{87}\text{Sr}$  optical lattice clocks beyond the SI limit, *Phys. Rev. Lett.* **114**, 230801 (2015).
- [18] X. Zheng, J. Dolde, H. M. Lim, and S. Kolkowitz, A lab-based test of the gravitational redshift with a miniature clock network, arXiv preprint arXiv:2207.07145 (2022).
- [19] M. Takamoto, I. Ushijima, N. Ohmae, T. Yahagi, K. Kokado, H. Shinkai, and H. Katori, Test of general relativity by a pair of transportable optical lattice clocks, *Nat. Photon* **14**, 411 (2020).
- [20] P. Delva, J. Lodewyck, S. Bilicki, E. Bookjans, G. Vallet, R. Le Targat, P.-E. Pottie, C. Guerlin, F. Meynadier, C. Le Poncin-Lafitte, *et al.*, Test of special relativity using a fiber network of optical clocks, *Phys. Rev. Lett.* **118**, 221102 (2017).
- [21] C. Lisdat, G. Grosche, N. Quintin, C. Shi, S. Raupach, C. Grebing, D. Nicolodi, F. Stefani, A. Al-Masoudi, S. Dörscher, *et al.*, A clock network for geodesy and fundamental science, *Nat. Commun.* **7**, 1 (2016).
- [22] M. Safronova, D. Budker, D. DeMille, D. F. J. Kimball, A. Derevianko, and C. W. Clark, Search for new physics with atoms and molecules, *Rev. Mod. Phys.* **90**, 025008 (2018).
- [23] D. Mitra, K. H. Leung, and T. Zelevinsky, Quantum control of molecules for fundamental physics, *Phys. Rev. A* **105**, 040101 (2022).
- [24] V. Andreev, D. G. Ang, D. DeMille, J. M. Doyle, G. Gabrielse, J. Haefner, N. R. Hutzler, Z. Lasner, C. Meisenhelder, B. R. O’Leary, C. D. Panda, A. D. West, E. P. West, and X. Wu (ACME Collaboration), Improved limit on the electric dipole moment of the electron, *Nature* **562**, 355 (2018).
- [25] W. B. Cairncross, D. N. Gresh, M. Grau, K. C. Cossel, T. S. Roussy, Y. Ni, Y. Zhou, J. Ye, and E. A. Cornell, Precision measurement of the electron’s electric dipole moment using trapped molecular ions, *Phys. Rev. Lett.* **119**, 153001 (2017).
- [26] X. Alauze, J. Lim, M. Trigatzis, S. Swarbrick, F. Collings, N. Fitch, B. Sauer, and M. Tarbutt, An ultracold molecular beam for testing fundamental physics, *Quantum Sci. Technol.* **6**, 044005 (2021).
- [27] O. Grasdijk, O. Timgren, J. Kastelic, T. Wright, S. Lamoreaux, D. DeMille, K. Wenz, M. Aitken, T. Zelevinsky, T. Winick, *et al.*, CeNTREX: A new search for time-reversal symmetry violation in the  $^{205}\text{Tl}$  nucleus, *Quantum Sci. Technol.* **6**, 044007 (2021).
- [28] N. R. Hutzler, Polyatomic molecules as quantum sensors for fundamental physics, *Quantum Sci. Technol.* **5**, 044011 (2020).
- [29] P. Yu and N. R. Hutzler, Probing fundamental symmetries of deformed nuclei in symmetric top molecules, *Phys. Rev. Lett.* **126**, 023003 (2021).
- [30] M. Germann, S. Patra, J.-P. Karr, L. Hilico, V. Korobov, E. Salumbides, K. Eikema, W. Ubachs, and J. Koelemeij, Three-body QED test and fifth-force constraint from vibrations and rotations of  $\text{HD}^+$ , *Phys. Rev. Res.* **3**, L022028 (2021).
- [31] E. Salumbides, J. Koelemeij, J. Komasa, K. Pachucki, K. Eikema, and W. Ubachs, Bounds on fifth forces from precision measurements on molecules, *Phys. Rev. D* **87**, 112008 (2013).
- [32] M. Borkowski, A. A. Buchachenko, R. Ciuryło, P. S. Julienne, H. Yamada, Y. Kikuchi, Y. Takasu, and Y. Takahashi, Weakly bound molecules as sensors of new gravitylike forces, *Sci. Rep.* **9**, 14807 (2019).
- [33] J. Kobayashi, A. Ogino, and S. Inouye, Measurement of the variation of electron-to-proton mass ratio using ultracold molecules produced from laser-cooled atoms, *Nat. Comm.* **10**, 3771 (2019).
- [34] D. Hanneke, B. Kuzhan, and A. Lunstad, Optical clocks based on molecular vibrations as probes of variation of the proton-to-electron mass ratio, *Quantum Sci. Technol.* **6**, 014005 (2020).
- [35] G. Barontini, L. Blackburn, V. Boyer, F. Butuc-Mayer, X. Calmet, J. C. Lopez-Urrutia, E. Curtis, B. Darquie, J. Dunningham, N. Fitch, *et al.*, Measuring the stability of fundamental constants with a network of clocks, *EPJ Quantum Technol.* **9**, 12 (2022).
- [36] T. Zelevinsky, S. Kotochigova, and J. Ye, Precision test of mass-ratio variations with lattice-confined ultracold molecules, *Phys. Rev. Lett.* **100**, 043201 (2008).
- [37] R. Oswald, A. Nevsky, V. Vogt, S. Schiller, N. Figueroa, K. Zhang, O. Tretiak, D. Antypas, D. Budker, A. Banerjee, *et al.*, Search for dark-matter-induced oscillations of fundamental constants using molecular spectroscopy, *Phys. Rev. Lett.* **129**, 031302 (2022).
- [38] I. Kozyryev, Z. Lasner, and J. M. Doyle, Enhanced sensitivity to ultralight bosonic dark matter in the spectra of the linear radical  $\text{SrOH}$ , *Phys. Rev. A* **103**, 043313 (2021).
- [39] A. M. Kaufman and K.-K. Ni, Quantum science with optical tweezer arrays of ultracold atoms and molecules, *Nat. Phys.* **17**, 1324 (2021).
- [40] J. T. Zhang, L. R. Picard, W. B. Cairncross, K. Wang, Y. Yu, F. Fang, and K.-K. Ni, An optical tweezer array of ground-state polar molecules, *Quantum Sci. Technol.* **7**, 035006 (2022).
- [41] S. Burchesky, L. Anderegg, Y. Bao, S. Y. Scarlett, E. Chae, W. Ketterle, K.-K. Ni, and J. M. Doyle, Rotational coherence times of polar molecules in optical tweezers, *Phys. Rev. Lett.* **127**, 123202 (2021).
- [42] K. Wang, C. P. Williams, L. R. Picard, N. Y. Yao, and K.-K. Ni, Enriching the quantum toolbox of ultracold molecules with Rydberg atoms, *PRX Quantum* **3**, 030339 (2022).
- [43] C. Zhang and M. Tarbutt, Quantum computation in a hybrid array of molecules and Rydberg atoms, *PRX Quantum* **3**, 030340 (2022).
- [44] N. B. Vilas, C. Hallas, L. Anderegg, P. Robichaud, A. Winnicki, D. Mitra, and J. M. Doyle, Magneto-optical trapping and sub-Doppler cooling of a polyatomic molecule, *Nature* **606**, 70 (2022).
- [45] V. V. Albert, J. P. Covey, and J. Preskill, Robust encoding of a qubit in a molecule, *Phys. Rev. X* **10**, 031050 (2020).
- [46] C. M. Tesch and R. de Vivie-Riedle, Quantum computation with vibrationally excited molecules, *Phys. Rev. Lett.* **89**, 157901 (2002).
- [47] E. Altman, K. R. Brown, G. Carleo, L. D. Carr, E. Demler, C. Chin, B. DeMarco, S. E. Economou, M. A. Eriksson, K.-M. C. Fu, *et al.*, Quantum simulators: Architectures and opportunities, *PRX Quantum* **2**, 017003 (2021).
- [48] S. A. Moses, J. P. Covey, M. T. Miecniowski, D. S. Jin, and J. Ye, New frontiers for quantum gases of polar molecules, *Nat. Phys.* **13**, 13 (2017).

- [49] A. L. Collopy, J. Schmidt, D. Leibfried, D. R. Leibbrandt, and C.-W. Chou, Rotational spectroscopy of a single molecular ion at sub part-per-trillion resolution, arXiv preprint arXiv:2207.10215 (2022).
- [50] S. S. Kondov, C.-H. Lee, K. H. Leung, C. Liedl, I. Majewska, R. Moszynski, and T. Zelevinsky, Molecular lattice clock with long vibrational coherence, *Nat. Phys.* **15**, 1118 (2019).
- [51] S. Patra, M. Germann, J.-P. Karr, M. Haidar, L. Hilico, V. Korobov, F. Cozijn, K. Eikema, W. Ubachs, and J. Koelemeij, Proton-electron mass ratio from laser spectroscopy of  $\text{HD}^+$  at the part-per-trillion level, *Science* **369**, 1238 (2020).
- [52] I. Kortunov, S. Alighanbari, M. Hansen, G. Giri, V. Korobov, and S. Schiller, Proton-electron mass ratio by high-resolution optical spectroscopy of ion ensembles in the resolved-carrier regime, *Nat. Phys.* **17**, 569 (2021).
- [53] P. K. Molony, A. Kumar, P. D. Gregory, R. Kliese, T. Puppe, C. R. Le Sueur, J. Aldegunde, J. M. Hutson, and S. L. Cornish, Measurement of the binding energy of ultracold  $^{87}\text{Rb}^{133}\text{Cs}$  molecules using an offset-free optical frequency comb, *Phys. Rev. A* **94**, 022507 (2016).
- [54] C.-F. Cheng, J. Hussels, M. Niu, H. Bethlem, K. Eikema, E. Salumbides, W. Ubachs, M. Beyer, N. Hölsch, J. Agner, *et al.*, Dissociation energy of the hydrogen molecule at  $10^{-9}$  accuracy, *Phys. Rev. Lett.* **121**, 013001 (2018).
- [55] M. Beyer, N. Hölsch, J. Hussels, C.-F. Cheng, E. J. Salumbides, K. S. Eikema, W. Ubachs, C. Jungen, and F. Merkt, Determination of the interval between the ground states of para-and ortho- $\text{H}_2$ , *Phys. Rev. Lett.* **123**, 163002 (2019).
- [56] J. Hussels, N. Hölsch, C.-F. Cheng, E. Salumbides, H. Bethlem, K. Eikema, C. Jungen, M. Beyer, F. Merkt, and W. Ubachs, Improved ionization and dissociation energies of the deuterium molecule, *Phys. Rev. A* **105**, 022820 (2022).
- [57] M. Takamoto, F.-L. Hong, R. Higashi, and H. Katori, An optical lattice clock, *Nature* **435**, 321 (2005).
- [58] A. D. Ludlow, M. M. Boyd, T. Zelevinsky, S. M. Foreman, S. Blatt, M. Notcutt, T. Ido, and J. Ye, Systematic study of the  $^{87}\text{Sr}$  clock transition in an optical lattice, *Phys. Rev. Lett.* **96**, 033003 (2006).
- [59] R. Le Targat, X. Baillard, M. Fouché, A. Bruschi, O. Tcherbakoff, G. D. Rovera, and P. Lemonde, Accurate optical lattice clock with  $^{87}\text{Sr}$  atoms, *Phys. Rev. Lett.* **97**, 130801 (2006).
- [60] F. Riehle, P. Gill, F. Arias, and L. Robertsson, The CIPM list of recommended frequency standard values: guidelines and procedures, *Metrologia* **55**, 188 (2018).
- [61] H. Jóźwiak and P. Weislo, Magic wavelength for a rovibrational transition in molecular hydrogen, *Sci. Rep.* **12**, 14529 (2022).
- [62] M. Tonouchi, Cutting-edge terahertz technology, *Nat. Photon* **1**, 97 (2007).
- [63] C. Wang, X. Yi, J. Mawdsley, M. Kim, Z. Wang, and R. Han, An on-chip fully electronic molecular clock based on sub-terahertz rotational spectroscopy, *Nat. Electron.* **1**, 421 (2018).
- [64] S. Nagano, M. Kumagai, H. Ito, Y. Hanado, and T. Ido, Terahertz frequency counter based on a semiconductor-superlattice harmonic mixer with four-octave measurable bandwidth and 16-digit precision, *Metrologia* **58**, 055001 (2021).
- [65] K. H. Leung, I. Majewska, H. Bekker, C.-H. Lee, E. Tiberi, S. Kondov, R. Moszynski, and T. Zelevinsky, Transition strength measurements to guide magic wavelength selection in optically trapped molecules, *Phys. Rev. Lett.* **125**, 153001 (2020).
- [66] L.-S. Ma, P. Jungner, J. Ye, and J. L. Hall, Delivering the same optical frequency at two places: Accurate cancellation of phase noise introduced by an optical fiber or other time-varying path, *Opt. Lett.* **19**, 1777 (1994).
- [67] B. Rauf, M. Vélez López, P. Thoumany, M. Pizzocaro, and D. Calonico, Phase noise cancellation in polarisation-maintaining fibre links, *Rev. Sci. Instrum.* **89**, 033103 (2018).
- [68] K. H. Leung, E. Tiberi, B. Iritani, I. Majewska, R. Moszynski, and T. Zelevinsky, Ultracold  $^{88}\text{Sr}_2$  molecules in the absolute ground state, *New J. Phys.* **23**, 115002 (2021).
- [69] R. Fasano, Y. Chen, W. McGrew, W. Brand, R. Fox, and A. Ludlow, Characterization and suppression of background light shifts in an optical lattice clock, *Phys. Rev. Appl.* **15**, 044016 (2021).
- [70] B. McGuyer, M. McDonald, G. Iwata, W. Skomorowski, R. Moszynski, and T. Zelevinsky, Control of optical transitions with magnetic fields in weakly bound molecules, *Phys. Rev. Lett.* **115**, 053001 (2015).
- [71] R. C. Brown, N. B. Phillips, K. Beloy, W. F. McGrew, M. Schioppo, R. J. Fasano, G. Milani, X. Zhang, N. Hinkley, H. Leopardi, *et al.*, Hyperpolarizability and operational magic wavelength in an optical lattice clock, *Phys. Rev. Lett.* **119**, 253001 (2017).
- [72] S. Jackson and A. C. Vutha, Magic polarization for cancellation of light shifts in two-photon optical clocks, *Phys. Rev. A* **99**, 063422 (2019).
- [73] V. Yudin, A. Taichenachev, M. Y. Basalaev, T. Zanon-Willette, J. Pollock, M. Shuker, E. A. Donley, and J. Kitching, Generalized autobalanced Ramsey spectroscopy of clock transitions, *Phys. Rev. Appl.* **9**, 054034 (2018).
- [74] T. Zanon-Willette, E. de Clercq, and E. Arimondo, Probe light-shift elimination in generalized hyper-Ramsey quantum clocks, *Phys. Rev. A* **93**, 042506 (2016).
- [75] T. Zanon-Willette, A. D. Ludlow, S. Blatt, M. M. Boyd, E. Arimondo, and J. Ye, Cancellation of stark shifts in optical lattice clocks by use of pulsed Raman and electromagnetically induced transparency techniques, *Phys. Rev. Lett.* **97**, 233001 (2006).
- [76] R. Hobson, W. Bowden, S. King, P. Baird, I. Hill, and P. Gill, Modified hyper-Ramsey methods for the elimination of probe shifts in optical clocks, *Phys. Rev. A* **93**, 010501 (2016).
- [77] S. G. Porsev and A. Derevianko, Multipolar theory of blackbody radiation shift of atomic energy levels and its implications for optical lattice clocks, *Phys. Rev. A* **74**, 020502 (2006).
- [78] C. Lisdat, J. V. Winfred, T. Middelmann, F. Riehle, and U. Sterr, Collisional losses, decoherence, and frequency shifts in optical lattice clocks with bosons, *Phys. Rev. Lett.* **103**, 090801 (2009).
- [79] K. Gibble and S. Chu, Laser-cooled Cs frequency standard and a measurement of the frequency shift due to ultracold collisions, *Phys. Rev. Lett.* **70**, 1771 (1993).
- [80] F. P. Dos Santos, H. Marion, S. Bize, Y. Sortais, A. Clairon, and C. Salomon, Controlling the cold collision shift

- in high precision atomic interferometry, *Phys. Rev. Lett.* **89**, 233004 (2002).
- [81] Y. Sortais, S. Bize, C. Nicolas, A. Clairon, C. Salomon, and C. Williams, Cold collision frequency shifts in a  $^{87}\text{Rb}$  atomic fountain, *Phys. Rev. Lett.* **85**, 3117 (2000).
- [82] T. Akatsuka, M. Takamoto, and H. Katori, Optical lattice clocks with non-interacting bosons and fermions, *Nat. Phys.* **4**, 954 (2008).
- [83] T. Akatsuka, M. Takamoto, and H. Katori, Three-dimensional optical lattice clock with bosonic  $^{88}\text{Sr}$  atoms, *Phys. Rev. A* **81**, 023402 (2010).
- [84] T. Takano, R. Mizushima, and H. Katori, Precise determination of the isotope shift of  $^{88}\text{Sr}$ – $^{87}\text{Sr}$  optical lattice clock by sharing perturbations, *Applied Physics Express* **10**, 072801 (2017).
- [85] S. Kato, R. Yamazaki, K. Shibata, R. Yamamoto, H. Yamada, and Y. Takahashi, Observation of long-lived van der Waals molecules in an optical lattice, *Phys. Rev. A* **86**, 043411 (2012).
- [86] Y. Yu, K. Wang, J. D. Hood, L. R. Picard, J. T. Zhang, W. B. Cairncross, J. M. Hutson, R. Gonzalez-Ferez, T. Rosenband, and K.-K. Ni, Coherent optical creation of a single molecule, *Phys. Rev. X* **11**, 031061 (2021).
- [87] I. S. Madjarov, A. Cooper, A. L. Shaw, J. P. Covey, V. Schkolnik, T. H. Yoon, J. R. Williams, and M. Endres, An atomic-array optical clock with single-atom readout, *Phys. Rev. X* **9**, 041052 (2019).
- [88] A. W. Young, W. J. Eckner, W. R. Milner, D. Kedar, M. A. Norcia, E. Oelker, N. Schine, J. Ye, and A. M. Kaufman, Half-minute-scale atomic coherence and high relative stability in a tweezer clock, *Nature* **588**, 408 (2020).
- [89] Bureau International des Poids et Mesures (BIPM), Circular T 414, (June 2022).
- [90] S. Preu, G. Döhler, S. Malzer, L. Wang, and A. Gossard, Tunable, continuous-wave terahertz photomixer sources and applications, *J. Appl. Phys.* **109**, 4 (2011).
- [91] F. Hindle, G. Mouret, S. Eliet, M. Guinet, A. Cuisset, R. Bocquet, T. Yasui, and D. Rovera, Widely tunable THz synthesizer, *Appl. Phys. B* **104**, 763 (2011).
- [92] S. Bartalini, L. Consolino, P. Cancio, P. De Natale, P. Bartolini, A. Taschin, M. De Pas, H. Beere, D. Ritchie, M. Vitiello, *et al.*, Frequency-comb-assisted terahertz quantum cascade laser spectroscopy, *Phys. Rev. X* **4**, 021006 (2014).
- [93] L. Consolino, F. Cappelli, M. S. de Cumis, and P. De Natale, QCL-based frequency metrology from the mid-infrared to the THz range: A review, *Nanophotonics* **8**, 181 (2019).
- [94] C. Daussy, F. Ducos, G. Rovera, and O. Acaf, Performances of  $\text{OsO}_4$  stabilized  $\text{CO}_2$  lasers as optical frequency standards near 29 THz, *IEEE transactions on ultrasonics, ferroelectrics, and frequency control* **47**, 518 (2000).
- [95] G. D. Rovera and O. Acaf, Optical frequency measurements relying on a mid-infrared frequency standard, in *Frequency measurement and Control* (Springer, 2001) pp. 249–272.
- [96] S. Stellmer, B. Pasquiou, R. Grimm, and F. Schreck, Creation of ultracold  $\text{Sr}_2$  molecules in the electronic ground state, *Phys. Rev. Lett.* **109**, 115302 (2012).
- [97] J. Aman, J. Hill, R. Ding, K. R. Hazzard, T. Killian, and W. Kon, Photoassociative spectroscopy of a halo molecule in  $^{86}\text{Sr}$ , *Physical Review A* **98**, 053441 (2018).
- [98] M. McDonald, *High precision optical spectroscopy and quantum state selected photodissociation of ultracold  $^{88}\text{Sr}_2$  molecules in an optical lattice* (Springer, 2017).
- [99] A. Stein, H. Knöckel, and E. Tiemann, The  $^1\text{S} + ^1\text{S}$  asymptote of  $\text{Sr}_2$  studied by Fourier-transform spectroscopy, *Eur. Phys. J. D* **57**, 171 (2010).
- [100] X. Zhang, K. Beloy, Y. Hassan, W. McGrew, C.-C. Chen, J. Siegel, T. Grogan, and A. Ludlow, Subrecoil clock-transition laser cooling enabling shallow optical lattice clocks, *Phys. Rev. Lett.* **129**, 113202 (2022).
- [101] T. Akatsuka, K. Hashiguchi, T. Takahashi, N. Ohmae, M. Takamoto, and H. Katori, Three-stage laser cooling of Sr atoms using the  $5s5p\ ^3P_2$  metastable state below Doppler temperatures, *Phys. Rev. A* **103**, 023331 (2021).
- [102] G. Reinaudi, C. Osborn, M. McDonald, S. Kotochigova, and T. Zelevinsky, Optical production of stable ultracold  $^{88}\text{Sr}_2$  molecules, *Phys. Rev. Lett.* **109**, 115303 (2012).
- [103] B. McGuyer, M. McDonald, G. Z. Iwata, M. Tarallo, A. Grier, F. Apfelbeck, and T. Zelevinsky, High-precision spectroscopy of ultracold molecules in an optical lattice, *New J. Phys.* **17**, 055004 (2015).
- [104] B. McGuyer, C. Osborn, M. McDonald, G. Reinaudi, W. Skomorowski, R. Moszynski, and T. Zelevinsky, Nonadiabatic effects in ultracold molecules via anomalous linear and quadratic Zeeman shifts, *Phys. Rev. Lett.* **111**, 243003 (2013).
- [105] M. McDonald, B. H. McGuyer, G. Z. Iwata, and T. Zelevinsky, Thermometry via light shifts in optical lattices, *Phys. Rev. Lett.* **114**, 023001 (2015).
- [106] K. D. Bonin and V. V. Kresin, *Electric-dipole polarizabilities of atoms, molecules, and clusters* (World Scientific, 1997).
- [107] W. Skomorowski, F. Pawłowski, C. P. Koch, and R. Moszynski, Rovibrational dynamics of the strontium molecule in the  $A^1\Sigma_u^+$ ,  $c^3\Pi_u$ , and  $a^3\Sigma_u^+$  manifold from state-of-the-art ab initio calculations, *J. Chem. Phys.* **136**, 194306 (2012).
- [108] H. Werner, P. Knowles, G. Knizia, F. Manby, M. Schütz, P. Celani, W. Györffy, D. Kats, T. Korona, R. Lindh, *et al.*, MOLPRO, version 2019.2, a package of ab initio programs, Cardiff, UK (2019).
- [109] A. Stein, H. Knöckel, and E. Tiemann, The states  $1^1\Sigma_u^+$ ,  $1^1\Pi_u$  and  $2^1\Sigma_u^+$  of  $\text{Sr}_2$  studied by Fourier-transform spectroscopy, *Eur. Phys. J. D* **64**, 227 (2011).
- [110] Joint Committee for Guides in Metrology, Evaluation of measurement data—Guide to the expression of uncertainty in measurement, *JCGM* **100**, 1 (2008).